Anisotropic charge transport in 2D single crystals of $Ti_3C_2T_x$ MXenes

Check for updates

Oriane de Leuze [1] ✉, Fernando Massa Fernandes [1], Sofiane Arib [1], Laura Caputo[1], Ana Pedro Fontes [1], Viet-Hung Nguyen [1], Hanna Pazniak[2], Bernard Nysten [1], Jean-Christophe Charlier [1], Sophie Hermans [1] & Benoît Hackens [1] ✉

Charge transport in two-dimensional crystals is critical for a large variety of future applications, and it is therefore highly desirable to get a better understanding of the underlying mechanisms. Here, we focus on the MXene $Ti_3C_2T_x$, which has recently garnered significant attention for its potential in printable electronics, energy storage and electromagnetic interference shielding, for which electrical properties play a leading role. To answer the need for experimental data on charge transport in $Ti_3C_2T_x$, we combine local-probe measurements (Conductive AFM), conventional four-contact measurements, finite element and ab initio simulations on individual few-layer flakes of $Ti_3C_2T_x$. This effort establishes new methods to study charge transport both in in-plane and out-of-plane directions and yields a consistent quantitative value of resistivity anisotropy in individual $Ti_3C_2T_x$ flakes, an essential ingredient in the understanding and modeling of charge transport in MXenes, in particular considering the role of interlayer interactions and surface functionalization in these materials.

By nature, multilayer materials composed of stacks of two-dimensional (2D) crystals held together by van der Waals forces, such as graphene, exhibit anisotropic properties[1,2]. While some methods can be readily devised to characterize properties like electrical conductivity along different axes of a bulk multilayer material[3,4], it is much more difficult to adapt such methods in the few-layer case as typical dimensions are in the μm (in-plane) and nm (out-of-plane) range. The common practice for electrical measurements on 2D flakes consists in the fabrication of devices with patterned contacts on the flakes, as shown in Fig. 1b–d, or transferring the 2D flakes on substrates with electrical contacts. Those techniques do not allow out-of-plane electrical measurements, making the study of anisotropic properties challenging for few-layer flakes. Yet, those properties are essential to characterize interlayer interactions, which are a key aspect in most applications using 2D crystals.

We focus here on MXenes, a family of 2D materials that garnered a lot of interest over the last few years. MXenes are 2D transition metal carbides, nitrides and carbonitrides, noted $M_{n+1}X_nT_x$, where n = 1, 2 or 3, 'M' is an early transition metal, 'X' is either C or N and T_x accounts for functional groups at the surface[5,6]. Their rich chemistry as well as surface terminations offer tunable electronic properties and surface engineering possibilities[7,8]. More specifically, functional groups can be controlled by the synthesis technique, making both the surface chemistry and the work function tunable[9]. For example, cation intercalation and physical delamination with solvent molecules used as intercalants have been studied towards inter-calation- and termination-engineered MXenes to gain control on inter- and

intra-flake transport mechanisms[10,11]. Structural and electronic modifications can also be induced in 2D MXenes by ion implantation[12,13]. On a larger scale, solution-processed films assembled from MXene nanosheets have numerous advantages, such as scalability, cost-effectiveness and compatibility with flexible substrates. In recent years, several strategies have been formulated to control the surface functional groups of MXene nanosheets to achieve the best balance between electron transport properties, atmospheric stability and dispersion in organic solvents[14]. Their versatility makes MXenes ideal for applications requiring specific chemical or electronic properties. Typically, they yielded breakthrough results in energy storage, electromagnetic interference shielding, sensing and printable electronics[14–19].

In the vast majority of applications using MXenes, flakes are spin-coated, drop-casted, printed or sprayed on various substrates, yielding random networks of overlapping individual flakes[20–22]. Electronic transport in those 2D networks is still a matter of debate in the case of MXenes: the intra- and inter-flake transport should be studied separately, and there is a lack of extensive experimental investigation of electronic transport in individual flakes in order to characterize 2D networks of MXenes[23,24]. Several works report on 2- and 4-contact electrical characterization of mono-layer and few-layer $Ti_3C_2T_x$ flakes, using conventional measurements on patterned devices[25–29]. However, as emphasized above, those techniques are not concluding for the characterization of anisotropic properties of individual flakes. A strong anisotropy of electrical resistivity, defined as $A = \frac{\rho_z}{\rho_{xx}}$,

[1]Institute of Condensed Matter and Nanosciences, UCLouvain, Louvain-La-Neuve, Belgium. [2]Laboratoire des Matériaux et du Génie Physique, Université Grenoble-Alpes, Grenoble, France. ✉e-mail: oriane.deleuze@uclouvain.be; benoit.hackens@uclouvain.be
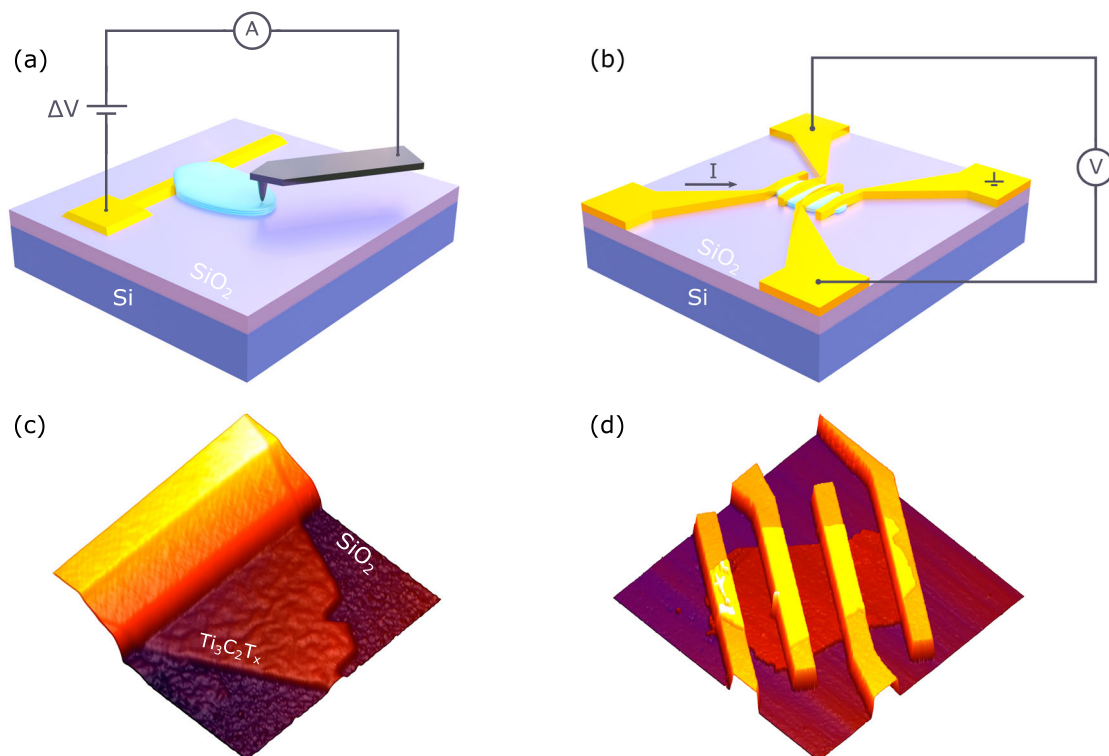
Fig. 1 | Electrical measurements on individual flakes with C-AFM and patterned contacts. a Illustration of C-AFM measurement on an individual flake deposited on a metallic electrode, on a Si/SiO$_2$ substrate. **b** Illustration of a conventional four-contact measurement on an individual flake. **c** 3D view of the AFM topography of a Ti$_3$C$_2$T$_x$ flake deposited partially on an electrode, obtained in tapping mode. **d** 3D view of the AFM topography of patterned contacts on a Ti$_3$C$_2$T$_x$ flake, obtained in tapping mode.

where ρ_z and ρ_{xx} are, respectively, the out-of-plane and in-plane resistivity, is reported in several MAX phases[3,30]. As MAX phases are the 3D precursors of MXenes, the study of anisotropy in their 2D counterpart is of utmost interest, in particular for 2D plasmonics[31]. Ab initio simulations have shown that the electronic conduction in Ti$_3$C$_2$(OH)$_2$ is highly anisotropic, and an experimental result on a Ti$_3$C$_2$T$_x$ particulate (i.e., a few μm-thick macroscopic aggregate of flakes) reports an estimated anisotropy of one order of magnitude[32]. No experimental reports have been published on anisotropy measurements on few-layer single-crystal individual flakes of MXenes, up to our knowledge.

In this context, advanced characterization at the nanoscale is needed to further explore charge transport in 2D MXenes. Scanning probe microscopy (SPM) tools are, in principle, the most adequate for this purpose, as the SPM probe size is typically in the few-nm range, much smaller than the lateral size of the flakes. Among the electrical SPM modes, Conductive Atomic Force Microscopy (C-AFM) offers high-resolution current maps and local current-voltage characterization at the nanoscale[33]. It is commonly used to study conduction mechanisms in 2D materials, current injection from contacts, and conductivity homogeneity[34–36]. Also, it allows for measuring out-of-plane current injection in 2D materials with the appropriate sample configuration, which makes it a method of choice to investigate the resistivity anisotropy in few-layer 2D crystals[37–39]. C-AFM is mostly used for qualitative measurements, as extracting quantitative data from SPM measurements is challenging. Indeed, as C-AFM is inherently a 2-contact technique, extrinsic electrical resistances come into play, whose relative contribution is not always straightforward to evaluate. Quantitative data can be extracted by combining the experimental results and an appropriate model, i.e., finite element simulations[40,41]. In the case of 2D crystals, electronic conductivity values were obtained from C-AFM measurements on electrochemically exfoliated graphene oxide and on monolayer CVD graphene using contact models[42,43]. In the case of MXenes, various SPM characterizations have been carried out, such as scanning thermal microscopy or Kelvin-probe force

microscopy (KPFM), but are rather sparse when it comes to C-AFM measurements[44]. Nevertheless, a recent study on perovskite solar cells incorporating MXenes highlighted the powerful capabilities of C-AFM for the study of nanoscale photoconduction[45].

In the present work, C-AFM measurements on flakes overlapping a metallic electrode and an insulating substrate are presented, as illustrated in Fig. 1a. A finite element model is used to simulate the electrostatics of a Ti$_3$C$_2$T$_x$ individual flake and infer its electronic resistivity from C-AFM current maps. The result is then compared to values obtained with conventional four-contact measurements on individual flakes, as illustrated in Fig. 1b. Combining C-AFM and finite element simulation results, we provide a quantitative estimate of the out-of-plane resistivity and, in turn, of the MXene electrical resistivity anisotropy. Lastly, the obtained anisotropy value is consistent with results from ab initio simulations results obtained on large MXene supercells incorporating different types of functional groups.

Results and discussion

In-plane resistivity of individual flakes, measured by C-AFM

First of all, C-AFM measurements on few-layer Ti$_3$C$_2$T$_x$ have been carried out in the configuration illustrated by Fig. 1a–c. In this case, an individual flake overlapping both the Au electrode and the SiO$_2$ substrate was selected for the measurement. The obtained C-AFM current map is shown in Fig. 2a, using a logarithmic color scale representing electrical current values for better contrast visualization. A 3-D image of the measured topography of the flake of interest is shown in the inset of Fig. 2b and can be used to correlate topography and current maps. Here, the average flake thickness t_z extracted from topography map is 12 nm, as shown in Supplementary Fig. 5. C-AFM current map allows to visualize the inhomogeneities in current distribution on the flake surface, which are partly related to tip-electrode distance and topography inhomogeneities. For example, one can notice in the current map of Fig. 2a that the flake edge exhibits less C-AFM current, which is directly linked to flake edge roughness that induces current

Fig. 2 | C-AFM measurement and simulation of the in-plane potential distribution on the flake.
a Current map of a C-AFM measurement on a $Ti_3C_2T_x$ flake overlapping a metallic electrode and an insulating substrate, obtained with a 5 mV bias. **b** Current values of the profile along the dashed line in (**a**). The inset shows a 3D view of the AFM topography of the flake and electrode. **c** Simulated potential distribution on the flake for C-AFM tip at 1.5 μm from the electrode, using C-AFM current at this location as input. **d** Comparison between the resistance profile extracted from the C-AFM measurements (orange line) and the resistance values on the flake as obtained from the simulation for different tip-electrode distances (stars).
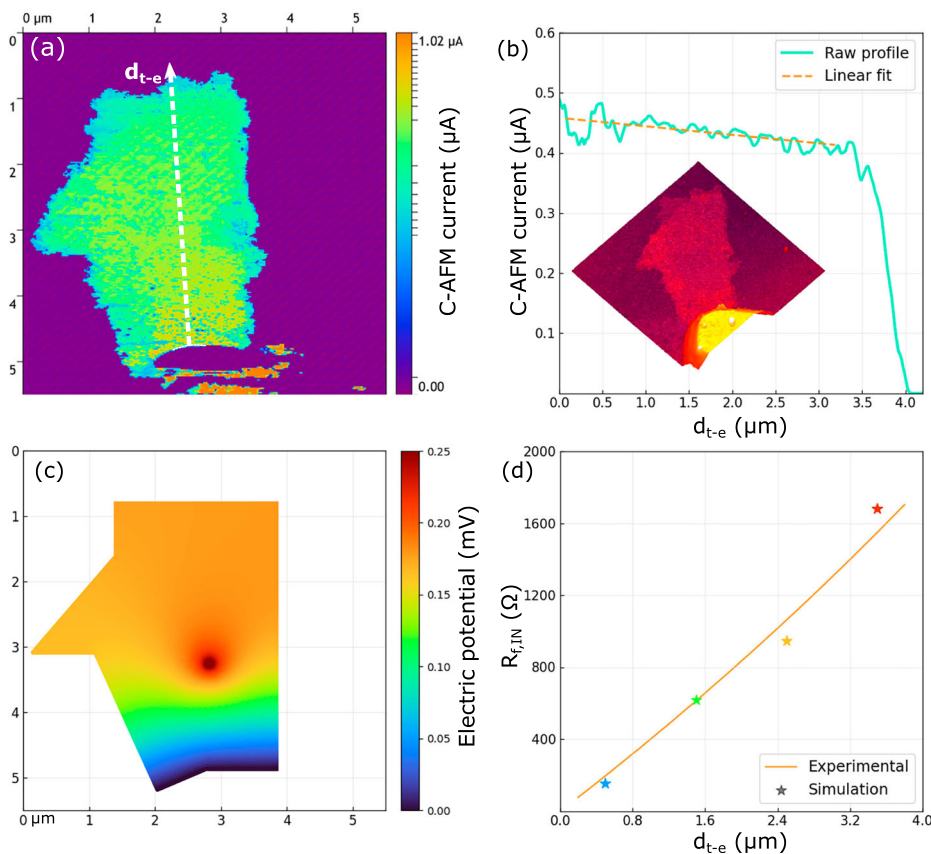
inhomogeneities. Here, we focus on the current evolution with the tip-electrode distance. For this specific C-AFM measurement configuration, the different contributions to the total measured resistance R_{TOT} can be expressed as follows:

$$R_{TOT} = \frac{\Delta V}{I_{AFM}} = R_{f,IN} + R_{f,OUT} + R_{C,tip} + R_{C,Au} \qquad (1)$$

In this expression, I_{AFM} is the measured C-AFM current, ΔV is the C-AFM bias voltage, $R_{f,IN}$ and $R_{f,OUT}$ are the in-plane and out-of-plane resistances of the flake, respectively. $R_{C,tip}$ represents the contact resistance between the tip and the flake and $R_{C,Au}$ is the contact resistance between the flake and the Au electrode. All those contributions are illustrated by Fig. 3a. $R_{f,IN}$ can be separated from other contributions to the total resistance thanks to its dependence on the tip-electrode distance, d_{t-e}. The latter is illustrated in Fig. 2a and is defined as the distance between the tip and the edge of the electrode, on the flake surface. Tip-electrode distance-induced C-AFM current variations can be studied more quantitatively by extracting a profile in the current map along the length of the flake. Figure 2b shows the current profile extracted along the white dashed line displayed on Fig. 2a. The location of the profile was chosen in an area where the flake topography is rather flat and homogeneous, to avoid any artifact related to tip interaction with topographical features. A gradient is observed on the extracted profile, as C-AFM current increases as the tip approaches the electrode, corresponding approximately to a linear variation of the in-plane resistance $R_{f,IN}$ as a function of d_{t-e}. Additional C-AFM results obtained on flakes of various thicknesses are shown in Supplementary Figs. 7, 8, with several current profiles where the linear dependence of the C-AFM current with d_{t-e} is also observed.

Next, we detail how fitting the current profile of Fig. 2b allows to separate the in-plane resistance from the other contributions to the resistance. First, the C-AFM current can be written as $I_{AFM} = I_0 + \alpha d_{t-e}$, where α is the slope of the current profile of Fig. 2b and I_0 is the C-AFM current

measured for $d_{t-e} = 0$. Then, the in-plane resistance can be rewritten $R_{f,IN}(d_{t-e}) = \frac{\Delta V}{I_0 + \alpha d_{t-e}} - (R_{f,OUT} + R_{C,tip} + R_{C,Au}) = \frac{\Delta V}{I_0 + \alpha d_{t-e}}$ - 10.85 kΩ. The goal is to extract the in-plane resistivity of the flake independently from contact resistances, as described in previous works on graphene[43,46]. First, we reproduce the geometry of the experiment, including the C-AFM tip, in a finite element simulation. This is necessary to capture the complexity of the electrostatics of a C-AFM measurement on a flake. Indeed, the simulated potential distribution in the flake, shown for $d_{t-e} = 1.5$ μm in Fig. 2c, is clearly not trivial (see Supplementary Fig. 4 for potential maps corresponding to other tip positions). We then adjust the flake resistivity ρ_{xx} in the simulation until the best match is found between the simulated $R_{f,IN}$ (at different d_{t-e}), and the experimentally obtained $R_{f,IN}(d_{t-e})$, as illustrated in Fig. 2d. The best fit was obtained for $\rho_{xx} = 6.81 \pm 0.91$ Ω μm, yielding good agreement between simulation points and experimental data, as presented in Fig. 2d.

Comparison with conventional 4-contact measurements on individual flakes

Besides C-AFM measurements on individual flakes, the electrical resistivity of similar flakes has also been extracted through more conventional four-contact measurements. The devices used for those measurements consist in $Ti_3C_2T_x$ flakes deposited on insulating substrate, with gold contacts patterned using lithography techniques, as illustrated by Fig. 1b–d. Several devices with at least four contacts on individual flakes have been fabricated and measured as described in the experimental section. Figure 4a shows optical micrographs of a $Ti_3C_2T_x$ flake and the as-fabricated device. As expected for metallic flakes, the obtained I-V characteristics are linear, as presented in Fig. 4b. Resistivity values were extracted from these measurements for each device and fall in the range of [1–20] Ω μm. The obtained values are represented as a function of flake thickness on Fig. 4c along with resistivity values of $Ti_3C_2T_x$ mono and few-layer flakes reported in the literature. The resistivity values obtained in the present work have been extracted taking into account flake geometry, and the error bars include the errors related to the geometry measurements from AFM topography as well as the noise of the resistance measurement. Note
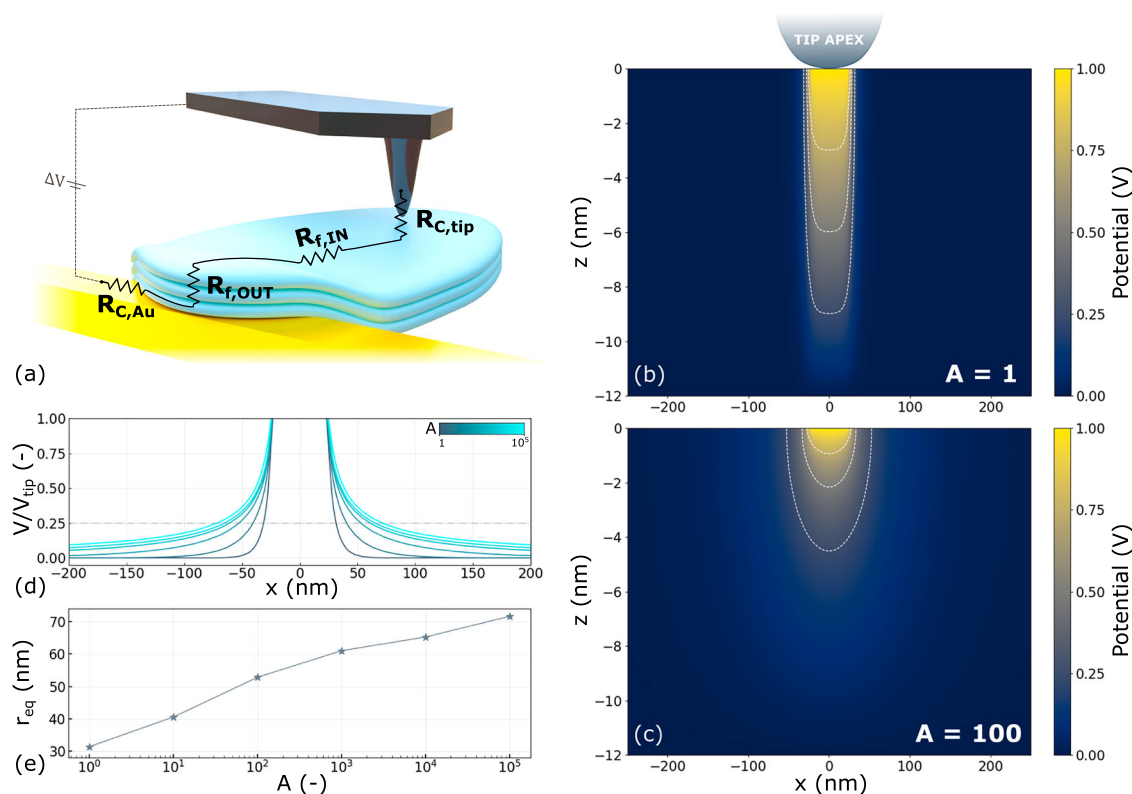
Fig. 3 | C-AFM equivalent circuit and simulated out-of-plane potential distribution in the flake. a Equivalent circuit of the C-AFM measurement on an individual few-layer flake. **b, c** Simulated potential distribution within the flake below the conductive tip for two different anisotropy values. **d** Simulated potential distribution at the flake surface, for various anisotropy values. **e** Simulation of the equivalent radius r_{eq} as a function of the anisotropy. r_{eq} is defined as the radius corresponding to the area where 75% of the potential drop occurs at the flake surface.

that the values reported by Lipatov et al. were acquired with two-contact measurements on MXenes synthesized by HF etching in one work[25] and by the MILD method for two other works[47,48]. Sang et al. also present two-contact measurements on MXenes synthesized with MILD method[27]. By contrast, Hemmat et al. report four-contact measurements on MXenes, also synthesized with MILD method, which is the closest situation compared to the present work[26]. Lastly, Shekhirev et al. also reported a resistivity value which belongs to the aforementioned range, with a four-contact measurement on an individual $Ti_3C_2T_x$ flake prepared via soft delamination[49]. It is interesting to note that even with different synthesis methods and when comparing measurements with two and four contacts, the resistivity values extracted are of the same order of magnitude. Consequently, contact resistance does not play a significant role in the measurements made on these devices, as Miranda et al. also indicated after control experiments[28]. It also proves that the resistivity of individual $Ti_3C_2T_x$ flakes is fairly stable for different synthesis and processing methods.

Figure 4c displays the resistivity value (ρ_{xx}, deduced from the measured R_{fIN}) obtained from the above-mentioned C-AFM measurement and simulation presented in Fig. 2. There is a remarkable agreement with the four-contact measurement approach, both in this work and in the literature. This, therefore, further validates the combined C-AFM and modeling approach for quantitative extraction of flake resistivity. As demonstrated in the present work, the C-AFM approach adds a degree of versatility that cannot be reached through conventional patterned contact measurements. One can indeed examine the local homogeneity of the flakes, as well as the decoupling between out-of-plane and in-plane components of the resistivity.

Resistivity anisotropy in $Ti_3C_2T_x$: from experimental results

Next, we focus on the extraction of $R_{f,OUT}$ from the C-AFM measurement to obtain ρ_z. To do so, the extrinsic contributions to R_{TOT} should be discussed. First, $R_{C,Au}$ is considered negligible compared to the total resistance, since it

was shown by Makaryan et al. that the MXene-Au contact resistance does not exceed 10-Ω with the transfer length method[50]. Also, similar work based on C-AFM measurements performed on epitaxial graphene reported a 2-Ω contact resistance between Au and graphene[35]. Then, I–V characteristics have been acquired with C-AFM on various locations on the Au electrodes (See Supplementary Fig. 6b) to estimate $R_{C,tip}$. The Au electrode is here considered as an ideal conductor and we assume that $R_{C,tip}$ stays in the same range whether the tip is located above the Au electrode or above $Ti_3C_2T_x$. This assumption is supported by the close values of work functions of both materials[51,52]. Indeed, KPFM measurements carried out in this work reveal that the work functions of Au and $Ti_3C_2T_x$ are in the same range, suggesting that the band-alignment in Pt/Ir and $Ti_3C_2T_x$ contact is comparable to the case of Pt/Ir and Au contact. Additional details can be found in Supplementary Fig. 9 and Supplementary Note 1. $R_{C,tip}$ is therefore estimated as 1390 ± 10 Ω. Using $R_{C,tip}$ estimation and neglecting $R_{C,Au}$, $R_{f,OUT}$ = 9.46 kΩ is obtained for the out-of-plane resistance of the flake.

Now that all the extrinsic contributions to the total resistance have been considered, the resistivity anisotropy can be written as follows:

$$A = \frac{\rho_z}{\rho_{xx}} = \frac{R_{f,OUT}\left(\frac{S_z}{t_z}\right)}{\rho_{xx}}, \qquad (2)$$

where S_z is the equivalent contact area under the tip and t_z is the flake thickness. Here, we use the value of ρ_{xx} = 6.81 ± 0.91 $\Omega\,\mu m$ found using C-AFM data combined with finite element simulations. To get an accurate view of the actual volume probed in this out-of-plane configuration, and hence an estimate of S_z, one has to rely again on a finite element simulation of the electrostatics of the vertical tip-MXene-contact geometry, as shown in Fig. 3d, e for different anisotropy values. Finite element simulations were proven to be well suited for quantitative interpretation of C-AFM
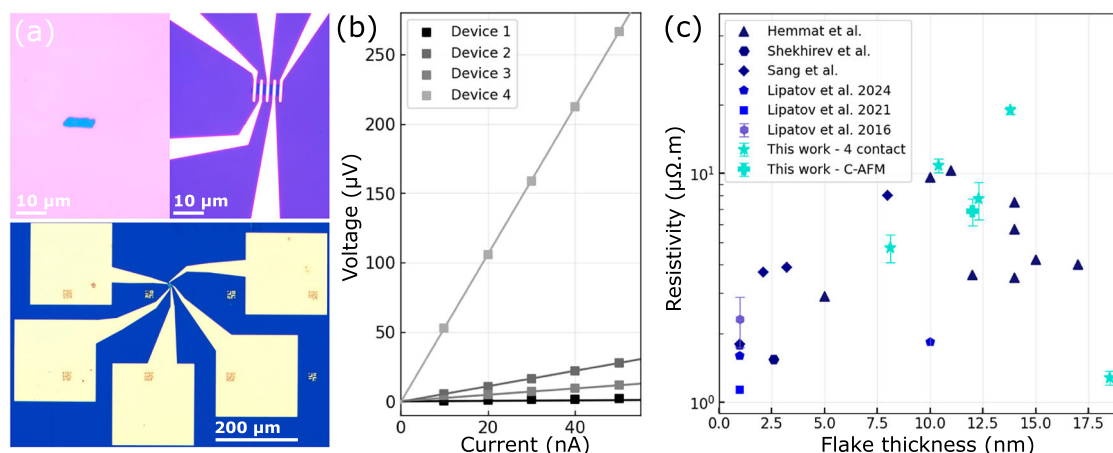
Fig. 4 | Individual flake resistivity measurements on patterned devices. a Optical microscope images of a $Ti_3C_2T_x$ flake and Au contacts patterned on the same flake. **b** V–I characteristics obtained with four-contact measurements on individual $Ti_3C_2T_x$ flakes. **c** In-plane resistivity values of $Ti_3C_2T_x$ individual flakes, combining this work and literature[25–27,47–49]. The datapoints for this work gather values from four-contact measurements on patterned devices and the resistivity value obtained using finite element simulation combined with C-AFM results, as described in Fig. 2. The error bars include the errors related to the geometry measurements from AFM topography, as well as the noise of the resistance measurement.

measurements on isotropic dielectric or semiconductor samples[40], but were never used with the same purpose in the case of metallic layered metals. Here, the model was established considering the 25-nm tip radius and equipotential layers of μm-range lateral length for the MXenes few-layer flakes. In this case, the simulated potential distribution shows that most of the potential drop occurs in the close vicinity of the tip apex, both for low and large anisotropy A, as shown on Fig. 3b, c. The equivalent contact area S_z is defined as the area where 75% of the potential drop occurs at the flake surface[33], with a radius noted r_{eq}. It has been simulated for a wide range of anisotropy values ($1–10^5$), and it appears that the evolution of r_{eq} with A is relatively slow, as shown on the graph of Fig. 3e. Based on these results, a range of [40–70] nm can therefore be used for r_{eq} as a first guess. As a consequence, we find from data in Fig. 2 that the obtained resistivity anisotropy range for this flake is $A = [510–2050]$, which can be refined to $A = 1400 \pm 200$ after several iterations to reduce r_{eq} interval according to finite element simulations of Fig. 3b–e. Such large anisotropy values are expected. Indeed, one knows that several MAX phases—the 3D precursors of MXenes—exhibit high resistivity anisotropy[3,4,30]. After the etching step, MAX phases undergo delamination steps to form MXenes, which are expected to exhibit even higher anisotropic properties than their 3D counterparts. Besides, the functional groups and intercalation of water between the MXene layers at ambient conditions are also major factors explaining the high resistivity anisotropy. The anisotropy dependence on intercalated species can precisely be exploited in sensing applications, as shown in the work of Loes et al., which studies the layer-dependent sensing mechanism of $Ti_3C_2T_x$[53].

To the best of our knowledge, no experimental data about resistivity anisotropy in $Ti_3C_2T_x$ individual flakes have been reported, so we can only compare our data with those of a small number of experimental reports on more macroscopic samples, where disorder and defects are likely to play prominent roles. A previous work reported a resistivity anisotropy of about one order of magnitude in an individual μm-thick $Ti_3C_2T_x$ particulate[32], which confirms experimentally the presence of resistivity anisotropy in $Ti_3C_2T_x$. For the case of a $Ti_3C_2T_x$ spray-coated layer, Makaryan et al. used impedance modeling to extract resistivity anisotropy, obtaining values between 10^5 and 10^7[50]. They also show a dependence of the anisotropy on the synthesis methods used to fabricate MXenes. While the aforementioned resistivity anisotropy values can not be directly compared to the specific case of individual flakes, they still indicate high resistivity anisotropy of $Ti_3C_2T_x$ despite the different morphologies considered. The case of a layer of flake is expected to showcase higher resistivity anisotropy values, as it also includes junction resistances between the flakes that are contributing to

electronic transport, mainly in the out-of-plane direction. The techniques used in the aforementioned studies are complementary, and C-AFM is a powerful addition to them as it allows for a more direct nanoscale measurement of the anisotropy at the individual flake level. It should also be noted that the resistivity anisotropy value obtained in this work is specific to few-layer flakes synthesized by the MILD method, measured under ambient conditions.

Resistivity anisotropy in $Ti_3C_2T_x$: from ab initio simulations

We provide another estimate of the electrical resistivity anisotropy through ab initio simulations. For this purpose, we consider the Ti_3C_2 supercell depicted in Fig. 5, which incorporates the main functional groups (-O, -OH, and -F) found in experimental samples. The resistivity anisotropy was estimated to be 440 as the ratio of the average out-of-plane resistivity to the average out-of-plane resistivity within an energy range of 1 eV at 300 K. One previous theoretical study shows that the electronic conduction in $Ti_3C_2(OH)_2$ is highly anisotropic[32]. In the latter case, and in general for theoretical works related to the electronic conduction in MXenes, the simulations are usually carried out while considering no functional group or one at a time, given the complexity of the system[54,55]. Herein, the mixture of functional groups considered in the supercell brings the simulation closer to experimental conditions. More specifically, as functional groups have a significant role in the out-of-plane transport, the conductivity anisotropy value is expected to be dependent on the surface chemistry. Indeed, varying the functional group proportion in the ab initio simulation, one obtains values of A up to 3000 when the proportion between -F, -O, and -OH groups is modified (See Supplementary Fig. 10). A major difference remaining with experimental conditions is the presence of water or other species adsorbed between individual crystal planes[56], which also influences the out-of-plane transport. Along with the uncertainty over the configuration of functional groups, water likely constitutes one of the main factors explaining the lower anisotropy value found in the simulation for similar proportions of functional groups in simulation and experiments. The value obtained in this ab initio simulation based on a realistic mixture of the main functional groups can therefore be safely used as a lower bound for resistivity anisotropy in $Ti_3C_2T_x$ in ambient conditions.

In summary, charge transport was investigated in $Ti_3C_2T_x$ individual flakes at the micro and nanoscale. To do so, conductive atomic force microscopy was performed on individual flakes overlapping a metallic electrode and an insulating substrate. The in-plane resistivity of a flake of interest could then be estimated to be around 7 ± 1 Ω μm thanks to an approach combining finite element simulations of the flake electrostatics
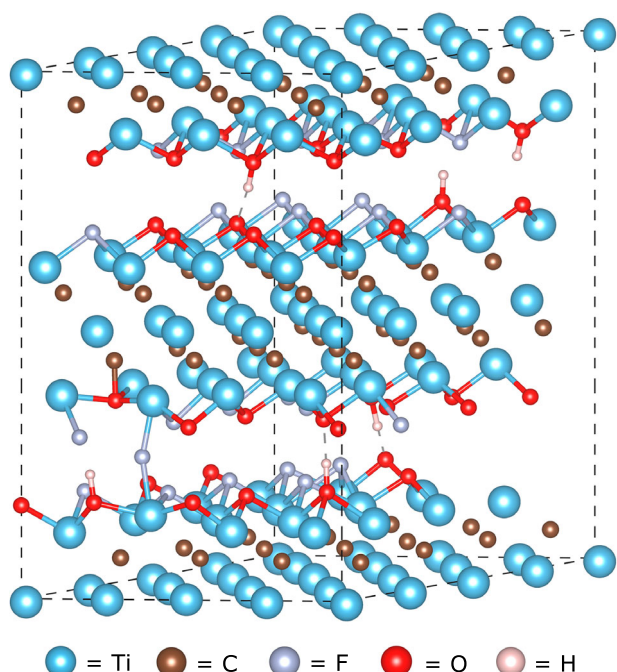
Fig. 5 | Ti₃C₂Tₓ supercell. Structurally-optimized atomistic model of $Ti_3C_2T_x$ supercell incorporating various functional groups with different concentrations: -OH (10%), -O (50%), and -F (40%).

with C-AFM data. Then, conventional four-contact measurements were performed on devices with contact patterns on top of individual $Ti_3C_2T_x$ flakes. The resistivities obtained for several individual flakes are in good agreement with previous works, and with the in-plane resistivity computed from the C-AFM measurement. This validates the C-AFM and finite element simulation approach to extract quantitative data, and therefore also offers interesting prospects towards quantitative real-space mapping of resistivity in other 2D crystals. Lastly, the specific configuration used for C-AFM measurements also allows for estimating the MXene out-of-plane resistivity and therefore to provide a quantitative measurement of the resistivity anisotropy in $Ti_3C_2T_x$ individual flakes around 10^3. Complementary ab initio simulations also allow to obtain an estimate of the high resistivity anisotropy in $Ti_3C_2T_x$, which is consistent with experiments. More generally, the study of charge transport at individual flake-scale provides invaluable insights to understand and model charge transport in a network of flakes more effectively and precisely. This work, therefore, paves the way for further investigations of the out-of-plane resistivity of different types of 2D crystals, which could prove important in various applications, such as understanding electrical contacts in all-2D-crystal transistors[57] or characterizing the effect of intercalation or functionalization on out-of-plane transport in 2D flakes.

Methods

Ti₃C₂Tₓ synthesis

$Ti_3C_2T_x$ was synthesized by the MILD (minimally intensive layer delamination) method from its MAX precursor, Ti_3AlC_2[58]. First, 1.6 g of LiF salt (Sigma-Aldrich, 99%) was dissolved in 20 mL HCl 9M (Sigma-Aldrich, 37%) and stirred in a Teflon beaker at room temperature for 10 min to obtain in situ HF. Then, 1 g Ti_3AlC_2 was gradually added to the solution over the course of 10 min. The etching solution was heated at 40 °C in an oil bath under constant stirring for 24 h, during which the Teflon beaker was covered by a lid. After etching, the suspension was washed multiple times with DI water using cycles of centrifugation and vortex mixing. Centrifugation cycles were carried out at 6000 rpm for 5 min and repeated until the pH of the supernatant approached 7. A black supernatant was observed after seven washing cycles, indicating the start of the delamination. The

$Ti_3C_2T_x$ slurry was then carefully collected above the $Ti_3C_2T_x$/Ti_3AlC_2 sediment and vacuum filtered with a 0.22 μm membrane filter. The obtained MXene film was left to dry overnight at room temperature and stored under an inert atmosphere. More details about the morphology of the as-synthesized film are presented in Supplementary Figs. 1, 2, along with a Raman spectrum of the same film.

Samples fabrication

$Ti_3C_2T_x$ flakes were deposited on two different substrates for this work. First, $Ti_3C_2T_x$ was drop-cast onto interdigitated electrodes (IDEs) with a digit width of 2 μm and a spacing of 5 μm between the digits. The IDEs were fabricated by photolithography followed by the evaporation of 20 nm Ti and 200 nm Au, as described by Afyouni et al.[59]. After $Ti_3C_2T_x$ drop casting and flake tracking, the 3 × 3 mm die was glued to a 1 cm² gold-coated plate and wedge bonding was performed using a gold wire to connect the contact pads of the IDEs to the plate, as shown in Supplementary Fig. 3. Secondly, for the four-contact measurements, $Ti_3C_2T_x$ flakes were drop-cast on a Si/SiO₂ substrate with alignment marks. Flakes with the most homogeneous aspect in optical micrographs and the largest sizes were selected for contact patterning. The contact patterns were created with electron beam lithography after spin-coating a 200 nm-thick PMMA layer and its soft bake. After pattern writing and developing with MIBK:IPA 1:3, a 5 nm layer of Ti and a 55 nm layer of Au were deposited by thermal evaporation. Lift-off was carried out using acetone.

In both cases, the flake concentration on the substrates can be adjusted depending on the time that the droplet remains in contact with the substrate. It is also possible to rehydrate the solid films collected after the synthesis to disperse the flakes in any solvent, DI water in this work. A 1-min sonication is then required to ensure proper dispersion, followed by a 15-min rest to allow sedimentation of unwanted agglomerated species before drop casting.

C-AFM measurements

C-AFM measurements were conducted with a Bruker Icon Dimension equipped with C-AFM module. Metal-coated tips with a radius of 25 nm (SCM-PIT-V2, Bruker) were used for the measurements. Such tips have a Pt/Ir conductive coating, an elastic constant of 3 N m⁻¹ and a resonance frequency of 75 kHz. The force applied on the tip was kept above 60 nN, as C-AFM current on $Ti_3C_2T_x$ flakes is force-dependent (See Supplementary Fig. 6a) and becomes constant above 60 nN. All the measurements were performed in air at room temperature. Gwyddion and NanoScope Analysis were used for C-AFM data analysis, as well as the pySPM library[60]. The finite element simulations were carried out using COMSOL Multiphysics.

Four-contact measurements

The measurements were done on patterned devices using a PM8 probe station and a lock-in amplifier at low frequency (79 Hz), which is needed to measure highly conductive samples while keeping low current values to prevent local damage or overheating.

Ab initio simulations

In order to theoretically estimate the ratio between the in-plane and out-of-plane conductivity, numerical simulations were conducted using the VASP code[61,62] within the density functional theory framework, employing the projector-augmented wave method and the PBE exchange-correlation functional[63,64]. Subsequently, a 4 × 4 × 2 supercell was constructed, and oxygen, fluorine, and hydroxyl groups were intercalated between the MXene layers using concentrations comparable with those reported in Benchakar et al. study for the case of the MILD method[8], which is consistent with the $Ti_3C_2T_x$ samples synthesized experimentally in this work. The structurally optimized atomistic model of Ti_3C_2 supercell incorporating various functional groups is shown in Fig. 5. After structural optimization, the in-plane and out-of-plane conductivity were calculated using the BoltzTraP2 code[65].

Data availability
The data that support the findings of the current study are available from the corresponding authors on reasonable request.

References
1. Gao, Z.-d et al. Anisotropic mechanics of 2d materials. *Adv. Eng. Mater.* **24**, 2200519 (2022).
2. Hermann, A., Somoano, R., Hadek, V. & Rembaum, A. Electrical resistivity of intercalated molybdenum disulfide. *Solid State Commun.* **13**, 1065–1068 (1973).
3. Ouisse, T. et al. Magnetotransport properties of nearly-free electrons in two-dimensional hexagonal metals and application to the m n + 1 a x n phases. *Phys. Rev. B* **92**, 045133 (2015).
4. Mauchamp, V. et al. Anisotropy of the resistivity and charge-carrier sign in nanolaminated Ti_2AlC: experiment and ab initio calculations. *Phys. Rev. B* **87**, 235105 (2013).
5. Naguib, M. et al. Two-dimensional nanocrystals produced by exfoliation of Ti_3AlC_2. *Adv. Mater.* **23**, 4248–53 (2011).
6. Naguib, M. et al. Two-dimensional transition metal carbides. *ACS Nano* **6 2**, 1322–31 (2012).
7. Agresti, A. et al. Titanium-carbide MXenes for work function and interface engineering in perovskite solar cells. *Nat. Mater.* **18**, 1–7 (2019).
8. Benchakar, M. et al. One max phase, different MXenes: a guideline to understand the crucial role of etching conditions on Ti_3C_2Tx surface chemistry. *Appl. Surf. Sci.* **530**, 147209 (2020).
9. Caffrey, N. M. Effect of mixed surface terminations on the structural and electrochemical properties of two-dimensional ti 3 c 2 t 2 and v 2 ct 2 mxenes multilayers. *Nanoscale* **10**, 13520–13530 (2018).
10. Hart, J. et al. Control of MXenes' electronic properties through termination and intercalation. *Nat. Commun.* **10**, 522 (2019).
11. Shi, S. et al. Recent advances in 2d mxenes: preparation, intercalation and applications in flexible devices. *J. Mater. Chem. A* **9**, 14147–14171 (2021).
12. Pazniak, A. et al. Ion implantation as an approach for structural modifications and functionalization of $Ti_3C_2T_x$ mxenes. *ACS Nano* **15**, 4245–4255 (2021).
13. Obrębowski, S. et al. Ion-implanted MXene electrodes for selective VOC sensors. *Appl. Mater. Today* **39**, 102343 (2024).
14. Ko, T. Y. et al. Functionalized MXene ink enables environmentally stable printed electronics. *Nat. Commun.* **15**, 3459 (2024).
15. Iqbal, A., Hassan, T., Madad, S., Gogotsi, Y. & Koo, C. M. Mxenes for multispectral electromagnetic shielding. *Nat. Rev. Electr. Eng.* **1**, 180–198 (2024).
16. Li, X. et al. Mxene chemistry, electrochemistry and energy storage applications. *Nat. Rev. Chem.* **6**, 389–404 (2022).
17. Wan, S. et al. Scalable ultrastrong MXene films with superior osteogenesis. *Nature* **634**, 1103–1110 (2024).
18. Iqbal, A., Hassan, T., Gao, Z., Shahzad, F. & Koo, C. M. Mxene-incorporated 1d/2d nano-carbons for electromagnetic shielding: a review. *Carbon* **203**, 542–560 (2022).
19. Devaraj, M., Rajendran, S., Hoang, T. K. & Soto-Moscoso, M. A review on MXene and its nanocomposites for the detection of toxic inorganic gases. *Chemosphere* **302**, 134933 (2022).
20. Jiang, X. et al. Inkjet-printed MXene micro-scale devices for integrated broadband ultrafast photonics. *npj 2D Mater. Appl.* **3**, 34 (2019).
21. Herber, M., Lengle, D., Valandro, S. R., Wehrmeister, M. & Hill, E. H. Bubble printing of Ti3C2Tx MXene for patterning conductive and plasmonic nanostructures. *Nano Lett.* **23**, 6308-6314 (2023).
22. Mojtabavi, M. et al. Wafer-scale lateral self-assembly of mosaic Ti_3C_2Tx mxene monolayer films. *ACS Nano* **15**, 625–636 (2021).
23. Gabbett, C. et al. Understanding how junction resistances impact the conduction mechanism in nano-networks. *Nat. Commun.* **15**, 4517 (2024).
24. Barsoum, M. W. & Gogotsi, Y. Removing roadblocks and opening new opportunities for MXenes. *Ceram. Int.* **49**, 24112–24122 (2023). A selection of papers presented at CIMTEC 2022.
25. Lipatov, A. et al. High electrical conductivity and breakdown current density of individual monolayer Ti3C2Tx MXene flakes. *Matter* **4**, 1413–1427 (2021).
26. Hemmat, Z. et al. Tuning thermal transport through atomically thin Ti3C2TZ MXene by current annealing in vacuum. *Adv. Funct. Mater.* **29**, 1805693 (2019).
27. Sang, X. et al. Atomic defects in monolayer titanium carbide (Ti3C2Tx) mxene. *ACS Nano* **10**, 9193–9200 (2016).
28. Miranda, A., Halim, J., Barsoum, M. & Lorke, A. Electronic properties of freestanding $Ti_3C_2T_x$ MXene monolayers. *Appl. Phys. Lett.* **108**, 033102 (2016).
29. Lipatov, A. & Sinitskii, A. Electronic and mechanical properties of MXenes derived from single-flake measurements. In: Anasori, B., Gogotsi, Y. (eds) *2D Metal Carbides and Nitrides (MXenes)* 301–325 (Springer, 2019).
30. Ouisse, T. & Barsoum, M. Magnetotransport in the max phases and their 2D derivatives: MXenes. *Mater. Res. Lett.* **5**, 1–14 (2017).
31. Raab, C., Rieger, J., Ghosh, A., Spellberg, J. L. & King, S. B. Surface plasmons in two-dimensional mxenes. *J. Phys. Chem. Lett.* **15**, 11643–11656 (2024).
32. Hu, T. et al. Anisotropic electronic conduction in stacked two-dimensional titanium carbide. *Sci. Rep.* **5**, 16329 (2015).
33. Rodenbücher, C., Wojtyniak, M. & Szot, K. *Conductive AFM for Nanoscale Analysis of High-k Dielectric Metal Oxides*, 29–70 (Springer, 2019).
34. Giannazzo, F., Greco, G., Roccaforte, F., Mahata, C. & Lanza, M. *Conductive AFM of 2D Materials and Heterostructures for Nanoelectronics*, 303–350 (Springer, 2019).
35. Giannazzo, F., Deretzis, I., La Magna, A., Roccaforte, F. & Yakimova, R. Electronic transport at monolayer-bilayer junctions in epitaxial graphene on SiC. *Phys. Rev. B* **86**, 235422 (2012).
36. Giannazzo, F., Schilirò, E., Greco, G. & Roccaforte, F. Conductive atomic force microscopy of semiconducting transition metal dichalcogenides and heterostructures. *Nanomaterials* **10**, 803 (2020).
37. Kubota, W., Utsunomiya, T., Ichii, T. & Sugimura, H. Local current mapping of electrochemically-exfoliated graphene oxide by conductive AFM. *Jpn J. Appl. Phys.* **59**, SN1001 (2020).
38. Giannazzo, F., Fisichella, G., Piazza, A., Agnello, S. & Roccaforte, F. Nanoscale inhomogeneity of the Schottky barrier and resistivity in MoS_2 multilayers. *Phys. Rev. B* **92**, 081307 (2015).
39. Chen, Z. et al. Vertical conductivity and topography in electrostrictive germanium sulfide microribbon via conductive atomic force microscopy. *Nano Lett.* **22**, 7636–7643 (2022).
40. Reid, O., Munechika, K. & Ginger, D. Space charge limited current measurements on conjugated polymer films using conductive atomic force microscopy. *Nano Lett.* **8**, 1602–9 (2008).
41. Villeneuve-Faure, C., Makasheva, K., Boudou, L. & Teyssedre, G. *Space Charge at Nanoscale: Probing Injection and Dynamic Phenomena Under Dark/Light Configurations by Using KPFM and C-AFM*, 267–301. https://doi.org/10.1007/978-3-030-15612-1_9 (Springer International Publishing, 2019).
42. Tu, Y., Utsunomiya, T., Ichii, T. & Sugimura, H. Enhancing the electrical conductivity of vacuum-ultraviolet-reduced graphene oxide by multilayered stacking. *J. Vac. Sci. Technol. B Nanotechnol. Microelectron. Mater. Process. Meas., Phenom.* **35**, 03D110 (2017).
43. Lim, S., Park, H., Yamamoto, G., Lee, C. & Suk, J. W. Measurements of the electrical conductivity of monolayer graphene flakes using conductive atomic force microscopy. *Nanomaterials* **11**, 2575 (2021). https://www.mdpi.com/2079-4991/11/10/2575.
44. Sahare, S. et al. An assessment of MXenes through scanning probe microscopy. *Small Methods* **6**, 2101599 (2022).

45. Panigrahi, S. et al. Mxene-enhanced nanoscale photoconduction in perovskite solar cells revealed by conductive atomic force microscopy. *ACS Appl. Mater. Interfaces* **16**, 1930–1940 (2023).

46. Nirmalraj, P., Lutz, T., Kumar, S., Duesberg, G. & Boland, J. Nanoscale mapping of electrical resistivity and connectivity in graphene strips and networks. *Nano Lett.* **11**, 16–22 (2011).

47. Lipatov, A., Bagheri, S. & Sinitskii, A. Metallic conductivity of Ti3C2T x MXene confirmed by temperature-dependent electrical measurements. *ACS Mater. Lett.* **6**, 298–307 (2023).

48. Lipatov, A. et al. Effect of synthesis on quality, electronic properties and environmental stability of individual monolayer Ti_3C_2 mxene flakes. *Adv. Electron. Mater.* **2**, 1600255 (2016).

49. Shekhirev, M. et al. Ultralarge flakes of Ti3C2Tx MXene via soft delamination. *ACS Nano* **16**, 13695–13703 (2022).

50. Makaryan, T., Okada, Y. & Suzuki, K. Impedance modeling for excluding contact resistance from cross-plane electronic conductivity measurement of anisotropic two-dimensional $Ti_3C_2T_x$ MXenes. *J. Appl. Phys.* **133**, 065304 (2023).

51. Kahn, A. Fermi level, work function and vacuum level. *Mater. Horiz.* **3**, 7–10 (2016).

52. Schultz, T. et al. Work function and energy level alignment tuning at Ti_3C_2Tx mxene surfaces and interfaces using (metal-) organic donor/acceptor molecules. *Phys. Rev. Mater.* **7**, 045002 (2023).

53. Loes, M. J., Bagheri, S. & Sinitskii, A. Layer-dependent gas sensing mechanism of 2d titanium carbide (Ti_3C_2Tx) mxene. *ACS Nano* **18**, 26251–26260 (2024).

54. Boussadoune, N., Nadeau, O. & Antonius, G. Electronic transport in titanium carbide MXenes from first principles. *Phys. Rev. B* **108**, 125124 (2023).

55. Khazaei, M. et al. Novel electronic and magnetic properties of two-dimensional transition metal carbides and nitrides. *Adv. Funct. Mater.* **23**, 2185–2192 (2013).

56. Ghidiu, M. et al. Ion-exchange and cation solvation reactions in Ti_3C_2MXene. *Chem. Mater.* **28**, 3507–3514 (2016).

57. Yuan, L. et al. Promises and prospects of two-dimensional transistors. *Nature* **591**, 43–53 (2021).

58. Bärmann, P. et al. Scalable synthesis of max phase precursors toward titanium-based mxenes for lithium-ion batteries. *ACS Appl. Mater. Interfaces* **13**, 26074–26083 (2021).

59. Afyouni, S., Enel, A., Hamoir, G. & Danlée, Y. An inkjet-printed rgo-pei composite for CO_2 monitoring working at room temperature. In: *Proc. IEEE International Symposium on Olfaction and Electronic Nose (ISOEN)*, 1–4 (IEEE, 2024).

60. Scholder, O. scholi/pyspm: pyspm v0.2.16 (version v0.2.16). https://doi.org/10.5281/zenodo.998575.

61. Kresse, G. & Furthmüller, J. Efficiency of ab-initio total energy calculations for metals and semiconductors using a plane-wave basis set. *Comput. Mater. Sci.* **6**, 15–50 (1996).

62. Kresse, G., & Furthmüller, J. Efficient iterative schemes for ab initio total-energy calculations using a plane-wave basis set. *Phys. Rev. B* **54**, 11–169 (1996).

63. Kresse, G. & Joubert, D. From ultrasoft pseudopotentials to the projector augmented-wave method. *Phys. Rev. b* **59**, 1758 (1999).

64. Perdew, J. P., Burke, K. & Ernzerhof, M. Generalized gradient approximation made simple. *Phys. Rev. Lett.* **77**, 3865 (1996).

65. Madsen, G. K. & Singh, D. J. Boltztrap. A code for calculating band-structure dependent quantities. *Comput. Phys. Commun.* **175**, 67–71 (2006).

Author contributions

O.D., F.M.F. and B.H. conceived and designed the experiments. O.D. and H.P. produced samples for analysis. O.D. and F.M.F. performed the experimental measurements. O.D., F.M.F. and S.A. carried out the data analysis and finite element simulations. L.C., A.P.F., V.N. and J.C. carried out ab initio simulations. O.D. and B.H. drafted the manuscript. F.M.F., S.A., L.C., A.P.F., V.N., H.P., B.N., J.C. and S.H. discussed the data, reviewed and edited the manuscript. B.H. supervised this study.

Competing interests

The authors declare no competing interests.

Additional information

Supplementary information The online version contains supplementary material available at https://doi.org/10.1038/s43246-025-00902-3.

Correspondence and requests for materials should be addressed to Oriane de Leuze or Benoît Hackens.

Peer review information *Communications Materials* thanks Filippo Giannazzo and the other, anonymous, reviewer(s) for their contribution to the peer review of this work. Primary Handling Editors: John Plummer. A peer review file is available.

Reprints and permissions information is available at http://www.nature.com/reprints

Publisher's note Springer Nature remains neutral with regard to jurisdictional claims in published maps and institutional affiliations.